BROOKHAVEN
NATIONAL LABORATORY

BNL-77329-2006-JA

Maps for Coupled Electron and Ion Clouds in Accelerators

Ubaldo Iriso and Stephen Peggs

Submitted to The American Physical Society

July 27, 2006

Superconducting Magnet Division

Brookhaven National Laboratory
P.O. Box 5000
Upton, NY 11973-5000
www.bnl.gov

Maps for coupled electron and ion clouds in accelerators

Ubaldo Iriso[1,*] and Stephen Peggs[1,†]

[1]*Consortium for the Exploitation of the Synchrotron Light Laboratory, P.O. Box 68, Bellaterra 08193, Spain*
[2]*Brookhaven National Laboratory, Upton, New York 11973, USA*

(Received 30 December 2005; published 27 July 2006)

Electron clouds sometimes limit accelerator performance by their appearance when the circulating bunch population exceeds a threshold value. Dynamical models of cloud buildup, and of the phase transition from ''cloud off'' to ''cloud on'', are enhanced when simple coupling between electron and ion clouds is included. Maps are then capable of reproducing the first order phase transitions sometimes seen in practice. They also predict that hysteresis, period doubling, and chaotic phenomena may be observed.

DOI: 10.1103/PhysRevSTAB.9.071002 PACS numbers: 29.20.Dh

I. INTRODUCTION

Quasistationary seed electrons in the vacuum pipe of an accelerator are accelerated in an impulse to an energy of order 1 keV when a bunch of positive particles passes by. These electrons strike the vacuum pipe wall, rapidly dissipating and diffusing into an electron spectrum that has a typical energy of only a few eV, until the next bunch passes by, when the process is iterated. Under some conditions electron multiplication occurs, and an electron cloud rapidly builds, until a stable dynamic equilibrium is attained. The necessary conditions include vacuum chamber surface characteristics [mainly given by the dependence of the secondary emission yield (SEY) on the incident electron energy], beam pipe geometry, and beam characteristics. For a given bunch spacing and for a particular beam pipe, electron clouds only build if the bunches have a large enough positive charge. Electron clouds have been observed in many accelerators, often acting as a fundamental limit to machine performance through dynamical instabilities, cryogenic heat loads, or unacceptably large associated vacuum pressure increases [1–4].

Electron cloud evolution is modeled with some significant success using complex simulation codes, typically tracking individual electrons or macroparticles, and sometimes employing 3-dimensional finite-element methods to calculate self-consistent forces and fields [5].

For the Relativistic Heavy Ion Collider (RHIC), it is found that the simulated evolution from the passage of bunch m to $m+1$ is empirically well represented by a cubic map [4,6]

$$\rho_{m+1} = a\rho_m + b\rho_m^2 + c\rho_m^3, \tag{1}$$

where ρ_m is the linear electron cloud density. Weak electron clouds grow exponentially in time if $a > 1$ since

$$\rho_m \approx \rho_0 a^m. \tag{2}$$

This exponential growth is finally limited due to the space charge forces of the electron cloud itself, and an equilibrium is obtained when

$$\rho_{m+1} = \rho_m \equiv \rho^*. \tag{3}$$

For example, if the cubic term in c is negligible, then the equilibrium electron density is

$$\rho^* = \begin{cases} 0; & \text{when } a < 1 \\ \frac{a-1}{-b}; & \text{when } a > 1. \end{cases} \tag{4}$$

Note a negative value of b is physically sensible, representing the self-limiting influence of accumulated (negative electron) space charge. Values for the electron cloud map coefficients are obtained from the empirical fits after running CPU intensive simulation codes [4,6].

An approximate analytical expression shows that the ''bunch to bunch electron cloud gain'' a can be interpreted as the effective SEY of the vacuum chamber [4]. It depends on: (1) the electron energy gain after the interaction with the bunch passage, (2) the electron multiplication after hitting the chamber wall, and (3) their survival until the next bunch passes by, when the process is iterated.

A. Phase transitions

What happens as the bunch population slowly decays away? Do the electron clouds collapse suddenly, or do they slowly fade away?

For a fixed set of beam pipe parameters, the coefficient a increases monotonically with the bunch population N, so that the stable electron cloud density $\rho^*(N)$ is also a function of bunch population [4,6]. Equation (4) then predicts that the phase transition from electron cloud ''off'' to ''on'' is second order—$\rho^*(N)$ increases smoothly from zero above a critical threshold population, when a becomes larger than unity. Complex simulation codes consistently reproduce only second order phase transitions [7].

Enhanced vacuum pressures are correlated with the direct observation of electron clouds. A linear relation exists between the vacuum pressure P and the linear electron flux into the wall, ϕ_e [8]. Furthermore, the latter can

*Electronic addresses: ubaldo@bnl.gov; ubaldo.iriso@cells.es
†Electronic address: peggs@bnl.gov

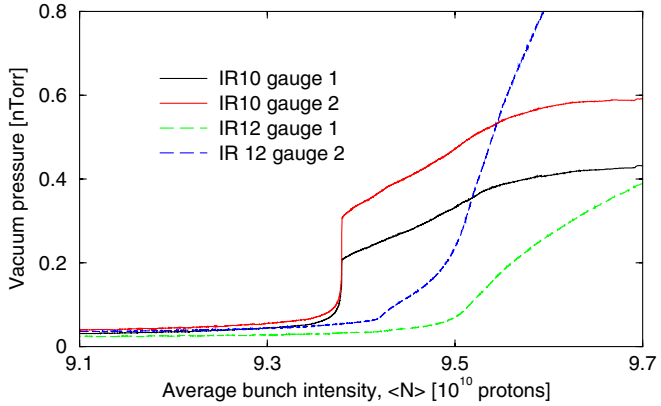

FIG. 1. (Color) First and second order electron cloud phase transitions observed in the interaction regions IR10 and 12 of the Relativistic Heavy Ion Collider. The data were taken as the bunch population slowly decayed during beam fill 5905. The actual copper ion bunch population is converted to an equivalent average number of protons per bunch.

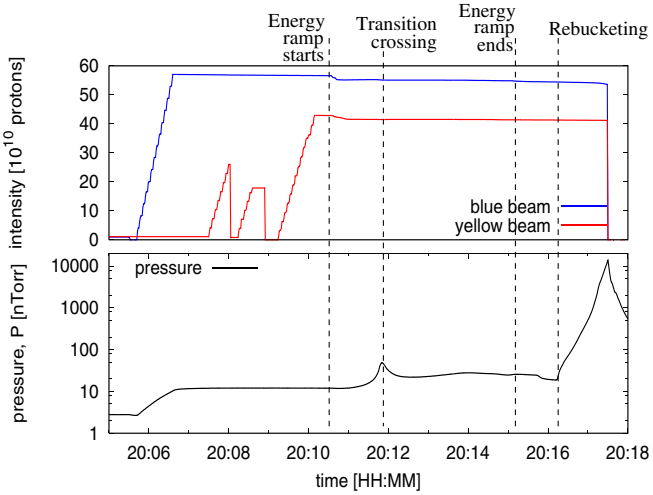

FIG. 2. (Color) A vacuum instability with gold beams in RHIC [13]. The upper plot shows the evolution of the beam intensity for both rings during injection, acceleration, and at the beginning of a store. The bottom plot shows the pressure instability that occurred in the collimator region of the blue ring when rf rebucketing significantly shrank the length of the circulating bunches.

also be related to the electron cloud density, ρ [9], so that

$$P \propto \phi_e \propto \rho. \tag{5}$$

Hence, a first order phase transition in the pressure corresponds to a first order phase transition in the electron cloud density, and vice versa.

However, experimental data shown in Fig. 1 illustrate how both first and second order phase transitions are seen in RHIC, as a threshold bunch population is crossed. While the pressure in IR12 smoothly decreases as the bunch population slowly drops, an abrupt transition is seen in IR10. This catastrophic collapse of the pressure is unexpected, especially since the surface parameters show a smooth dependence on the impact electron energy at the wall [10,11]. The failure of simulations to reproduce these first order phase transitions, and of theory to predict them, indicates that there is missing physics in the modeling.

B. Ion clouds

A candidate for additional physics is the interplay between electron clouds and positive ion clouds. An initial analysis of the Large Hadron Collider (LHC) in Ref. [12] concluded that this interplay would not significantly affect accelerator performance. Nonetheless, it is introduced to explain experimental observations at RHIC [13], and more recently it has been reconsidered for the LHC [14].

Figure 2 depicts a pressure instability in the unbaked collimator region at RHIC, where "L shaped" copper blocks are placed in a chamber with larger aperture than IR10 and IR12. The instability shows a slow exponential growth (growth time, $\tau_g \approx 10$ s) that occurs when the bunch length is reduced by rf rebucketing. A bunch length reduction increases the electron density [4,8]. This points towards the existence of a feedback mechanism in which the pressure is crucially involved. This instability is probably caused by partial ionization of the rest gas by the beam and the electron cloud, and it is described by [13]

$$P = \frac{Q_0 + \eta_e k T L \phi_e / e}{S - \eta_{\mathrm{ion}} L b_0}, \tag{6}$$

where Q_0 is the static gas load, η_e is the electron induced molecular desorption coefficient, k is Boltzmann's constant, T is the temperature, e is the absolute electron charge, $2L$ is the distance between two consecutive vacuum pumps, $2S$ is the pumping speed, and η_{ion} is the ion induced molecular desorption coefficient. The parameter b_0 is given by [13]

$$b_0 = (\sigma_e d \phi_e + \sigma_b I_b)/e, \tag{7}$$

where σ_e is the cross section for rest gas ionization from an impact of cloud electrons, d is the beam pipe diameter, σ_b is the cross section for rest gas ionization by the beam, and I_b is the beam current.

Models of this interplay face two main challenges: a significant number of uncertain surface physics parameters for both electron and ions, and extremely different time scales for electron and ion cloud dynamics. Long ion lifetimes imply very long CPU times for simulations. Not only is the typical time of flight between surfaces much longer for a massive ion than for an electron of similar kinetic energy, but also the backscattering probability for ion energies below ~30 eV is close to unity [15]. The lifetime of such ions is not only characterized by their time of flight, but also by vacuum pumping times that are often measured in seconds. Therefore, electron clouds evolve with a time

scale on the order of 1 μs, while ion clouds evolve between three and six orders of magnitude more slowly.

Next, we show how maps can be used to circumvent these challenges and give an improved intuitive understanding of the coupled evolution of electron and ion clouds. Coupled maps also show how, at least in principle, first order phase transitions can occur.

II. COUPLED MAPS AND FIXED POINTS STABILITY

In a map model, the interplay between electron clouds and ion clouds is generally expressed by

$$\rho_{m+1} = f(\rho_m, R_m) \tag{8}$$

$$R_{m+1} = g(\rho_m, R_m), \tag{9}$$

where R_m is the linear ion cloud density after the passage of the mth bunch. Both ρ_m and R_m are defined to be positive, and their convenient units are (nC/m).

In the following, we use the vector $\vec{r}$ for the electron and ion densities

$$\vec{r}_m = \begin{pmatrix} \rho_m \\ R_m \end{pmatrix}. \tag{10}$$

A fixed point is found when

$$\vec{r}_{m+1} = \vec{r}_m \equiv \vec{r}^*, \tag{11}$$

that is to say, when

$$\rho_{m+1} = \rho_m \equiv \rho^*, \qquad R_{m+1} = R_m \equiv R^*. \tag{12}$$

Furthermore, we need the fixed point to be *stable*. That is, small perturbations around the fixed point $\vec{r}^*$ must result in an evolution that converges towards the fixed point.

Close to a fixed point $\vec{r}^*$, the linear motion in one time step from bunch passage m to $m+1$ is

$$\vec{r}_{m+1} = J\vec{r}_m, \tag{13}$$

where J is the 2×2 Jacobian matrix

$$J = \begin{pmatrix} \frac{\partial f}{\partial \rho_m} & \frac{\partial f}{\partial R_m} \\ \frac{\partial g}{\partial \rho_m} & \frac{\partial g}{\partial R_m} \end{pmatrix}_{\vec{r}^*} \tag{14}$$

that determines the stability of the fixed point through its trace and determinant. Appendix A shows that a fixed point is stable if one of the two following pairs of conditions is fulfilled:

$$\text{(i)} \quad t^2 < d^2; \qquad \text{and} \quad d^2 < 1 \tag{15}$$

$$\text{(ii)} \quad t^2 > d^2; \qquad \text{and} \quad |t| + \sqrt{t^2 - d^2} < 1, \tag{16}$$

where the convenient definitions

$$t \equiv \mathrm{Tr}(J^2)/2 \tag{17}$$

$$d \equiv \det(J) \tag{18}$$

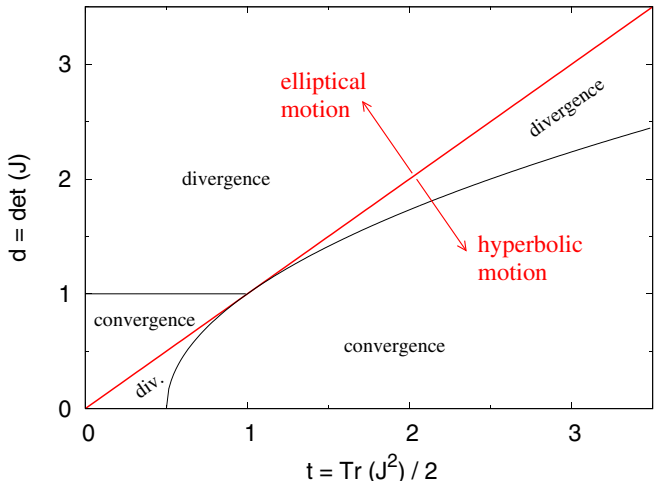

FIG. 3. (Color) Stability regions as a function of the parameters t and d [Eqs. (17) and (18)], obtained from the Jacobian matrix. Above the 45° line the motion shows elliptical behavior, while below it the motion is hyperbolic.

have been introduced. If neither of these conditions applies, then the motion diverges. Appendix A shows, moreover, that two different motions can be obtained around the fixed points: elliptical or hyperbolic. Figure 3 shows the stability regions in (t, d) space. Note that these stability conditions are valid for any form of the functions f and g, representing a broad spectrum of potential coupling mechanisms.

III. A SIMPLE COUPLED MAPS MODEL

In order to visualize the phenomena that these conditions can generate, we use an example for the functions f and g based on the cubic map for the electron density [Eq. (1)]. Consider the "proof-of-principle" coupled maps

$$\rho_{m+1} = (a + yR_m)\rho_m + b\rho_m^2 + c\rho_m^3 \tag{19}$$

$$R_{m+1} = AR_m + Y\rho_m. \tag{20}$$

If the coupling coefficients are turned off ($y = Y = 0$), then the electron cloud map Eq. (1) is recovered, along with the uncoupled ion map

$$R_{m+1} = AR_m. \tag{21}$$

Values of A slightly larger than unity correspond to an exponential growth (as in Fig. 2), while values smaller than unity correspond to ion cloud clearance, for example, through vacuum pumping and neutralization. Since massive ion clouds only clear slowly, we expect $A \approx 1$.

There are two coupling mechanisms in Eqs. (19) and (20):

(1) Electrons generate a positive ion cloud by colliding with the rest gas in the vacuum chamber. This is represented by the term $Y\rho_m$ in Eq. (20). Y is

TABLE I. Map parameters used in the following examples.

a	b	c	y	A	Y
Equation (27)	−0.1	−0.08	0.4	0.96	0.03

positive, but its order of magnitude is not trivially apparent.

(2) The slow moving positive ions enhance the probability of electron survival between one bunch passage and the next. This is represented by the term yR_m, and has been written in Eq. (19) as an addition to the linear bunch to bunch gain a. Moreover, the presence of an ion cloud also tends to neutralize the negative electron space charge of the accumulated electron cloud. This is stressed rewriting Eq. (19) as

$$\rho_{m+1} = a\rho_m + (yR_m + b\rho_m)\rho_m + c\rho_m^3. \quad (22)$$

For these reasons, physical values of y are positive, typically smaller than a, and of the same magnitude as b, so $y < a$ and $y \sim |b|$.

In this example, the electron cloud densities at the fixed points correspond to the roots of the cubic equation

$$\rho^* = a\rho^* + b'\rho^{*2} + c\rho^{*3}, \quad (23)$$

where the ''effective space charge coefficient''

$$b' = b - [yY/(A-1)] \quad (24)$$

has been conveniently introduced. One of the 3 roots ($\rho^* = 0$) is trivial. The 2nd and 3rd roots,

$$\rho^* = \frac{-b' \pm \sqrt{b'^2 - 4c(a-1)}}{2c} \quad (25)$$

are only physical if their values are real and positive.

Finally, the stationary ion density is simply related to the stationary electron density by

$$R^* = -\frac{Y}{A-1}\rho^* \quad (26)$$

[recall that Y is positive and $(A-1)$ is negative].

A. Numerical application

Next, we assume that all the coupled map coefficients are constants except for the bunch to bunch electron cloud gain, a. From the fitting results in Refs. [4,6], we presume that a depends linearly on the bunch population according to

$$a = 0.4 + 0.1(N/10^{10}). \quad (27)$$

The coupled map coefficient values used throughout below and quoted in Table I are illustrative—they are not intended to quantitatively reproduce RHIC results.

The right-hand side of Eq. (23) is plotted in Fig. 4 for three bunch populations. The fixed point solutions are found where these curves intersect with the left-hand side of Eq. (23)—that is, the *identity map* or the 45° line. Figure 4 shows that three fixed electron densities exist for $N = 5.0 \times 10^{10}$ protons/bunch: $\rho_1^* = 0$ nC/m, $\rho_2^* = 0.69$ nC/m, and $\rho_3^* = 1.81$ nC/m. Calculating the Jacobian matrix at the three solutions, their corresponding stability is obtained using Eqs. (15) and (16):

(1) The first fixed point $\vec{r}^*_1 = (0, 0)$ shows
  (i) $t^2 < d^2 \rightarrow$ elliptic motion
  (ii) $d^2 < 1 \rightarrow$ convergence
  as shown in the left plot of Fig. 5.

(2) The second fixed point $\vec{r}^*_2 = (0.69, 0.52)$ shows
  (i) $t^2 > d^2 \rightarrow$ hyperbolic motion
  (ii) $|t| + \sqrt{t^2 - d^2} > 1 \rightarrow$ divergence
  as shown in the middle plot of Fig. 5.

(3) The third fixed point $\vec{r}^*_3 = (1.81, 1.357)$ shows
  (i) $t^2 > d^2 \rightarrow$ hyperbolic motion
  (ii) $|t| + \sqrt{t^2 - d^2} < 1 \rightarrow$ convergence
  as shown in the right plot of Fig. 5.

Note that Eq. (27) sets $a = 0.9 < 1$ for $N = 5 \times 10^{10}$ protons/bunch. According to the first order uncoupled map [Eq. (2)], this does not produce any electron cloud (stable or unstable). However, the presence of a coupled ion cloud enhances the electron survival, and stable and nonzero electron clouds are created even when $a < 1$. Enhanced electron survival due to the presence of an ion cloud is also considered in Ref. [16], but the ion cloud density is not allowed to evolve.

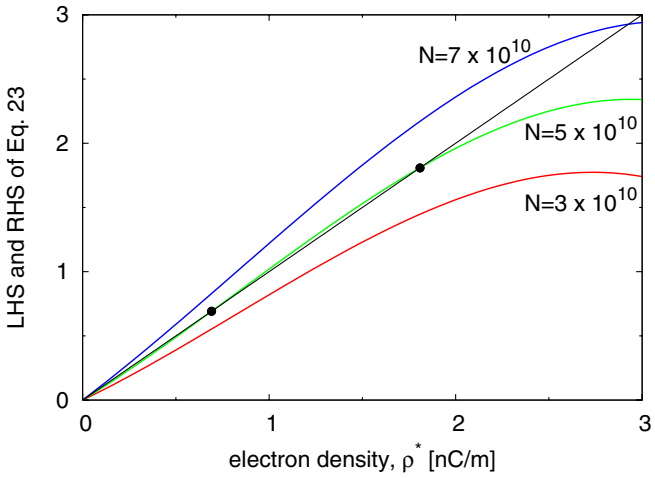

FIG. 4. (Color) Three different representations of the right-hand side (RHS) of Eq. (23) corresponding to $N = 3$, 5, and $N = 7 \times 10^{10}$ protons/bunch. The straight line shows the left-hand side (LHS) of Eq. (23). Intersections between the RHS and LHS of Eq. (23) mark the stationary electron densities. Two nonzero solutions exist for $N = 5 \times 10^{10}$ protons/bunch: at $\rho^* = 0.69$ and $\rho^* = 1.81$ nC/m. Their stability is examined in Fig. 5.

B. First order phase transitions and hysteresis

These conditions lead to a first order phase transition, and to hysteresis. Figure 6 shows the results of a dynamical

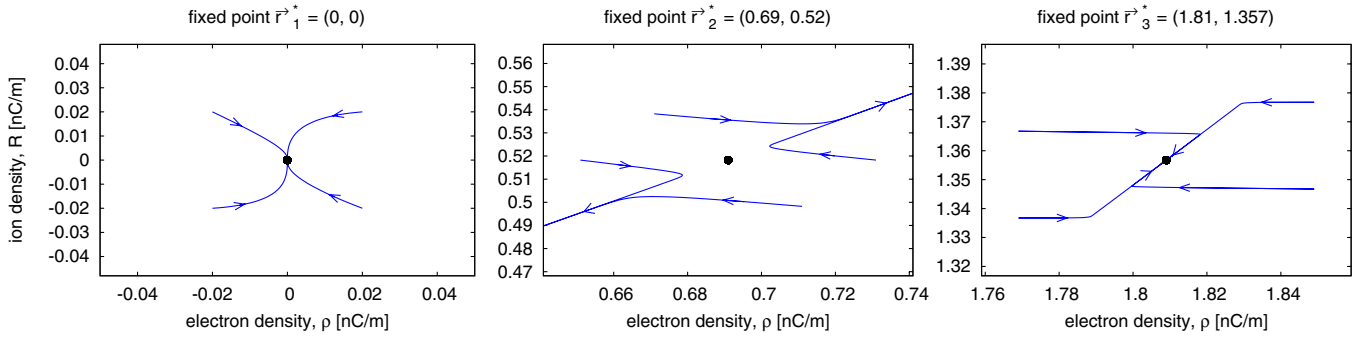

FIG. 5. (Color) Stability around the 3 fixed points for $N = 5 \times 10^{10}$ protons/bunch. The first solution (left) shows an elliptical converging motion. The second solution (middle plot) shows a hyperbolic diverging motion, through which small perturbations around the fixed point $\vec{r}^*_2$ diverge quickly towards $\vec{r}^*_1$ or $\vec{r}^*_3$, depending on the initial conditions. The third solution (right) shows a hyperbolic converging motion that attracts all the points in its vicinity. Recall that only trajectories with positive ρ, R are physically sensible; the motion depicted around $\vec{r}^*_1$ includes negative values of ρ and R only as a numerical example. Fixed points $\vec{r}^*_1$ and $\vec{r}^*_3$ are *attractors*, while $\vec{r}^*_2$ is a *repeller*.

simulation, in which the coupled maps are applied directly, first as the bunch population is slowly decreased, and then as it is slowly increased. The solid line shows that the stable electron cloud density decreases as the bunch population is reduced, until at $N \approx 4.7 \times 10^{10}$ the electron cloud collapses catastrophically. When the bunch population is then slowly increased, no electron (or ion) cloud forms up to a population of $N = 6.0 \times 10^{10}$, when the cloud grows rapidly to a stable stationary value.

Figure 7 shows the flow in (ρ, R) space for different bunch populations: $N = 3, 5$, and 7×10^{10} protons/bunch. These plots result from tracking several simulations with different initial conditions. For $N = 3 \times 10^{10}$ (left plot), all trajectories are attracted to the *global attractor* at the $\vec{r}^* = (0, 0)$ fixed point. Similar behavior is found for $N = 7 \times 10^{10}$ (right plot), where all trajectories converge to the *global attractor* at $\vec{r}^* = (2.9, 2.17)$, no matter what initial conditions are used. Note that there is also a fixed point *global repeller* at $\vec{r}^* = (0, 0)$.

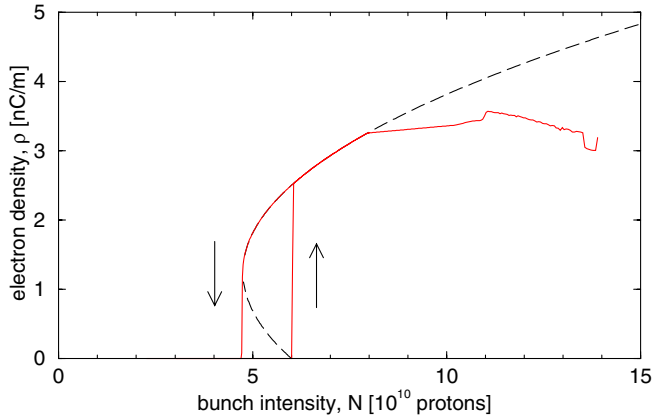

FIG. 6. (Color) Evolution of the electron cloud density as the bunch population N is first slowly decreased, and then slowly increased. The precipitous and hysteretic behavior is characteristic of first order phase transitions. The dashed lines represent the two stationary solutions described in Eq. (25).

However, the situation is different for $N = 5 \times 10^{10}$ protons/bunch (middle plot in Fig. 7). Two different *basins of attraction* coexist: one corresponding to the fixed point $\vec{r}^* = (0, 0)$, the second corresponding to the fixed point $\vec{r}^* = (1.81, 1.357)$. This feature is the origin of the hysteresis and the first order phase transitions. The boundary between the two basins moves to the upper right of the plot as the bunch population smoothly decreases below $N = 5.0 \times 10^{10}$, until the two nonzero fixed points coincide at about $N = 4.7 \times 10^{10}$ protons/bunch. At this point the second basin disappears, and all trajectories collapse to $\vec{r}^* = (0, 0)$, no matter what their initial conditions.

In this model the presence of either first or second order phase transitions depends on the values of the map coefficients, which produce ion cloud densities comparable to electron cloud densities, $\rho \sim R$. The coefficients have been adjusted to show how first order phase transitions may come about (as in Fig. 1, IR10), but they can also be adjusted to reproduce second order phase transitions (as in Fig. 1, IR12), or the slow indefinite growth (as in the collimator region in the blue ring in Fig. 2). It is only necessary to postulate that the different materials and geometries in the different RHIC sections produce different values for the map coefficients (different desorption coefficients, SEY, etc.).

The importance of the model stems from its ability to show the possibility of abrupt transitions even with a smooth dependence of the map coefficients on electron cloud parameters (such as bunch population or length). Recall that all coefficients remain constants except a, which changes linearly with the bunch intensity.

IV. ADDITIONAL DYNAMICAL PHASES

The coupled map difference equations can be rewritten

$$\Delta\rho/\Delta t = [(a - 1) + b\rho + yR]\rho + c\rho^3 \qquad (28)$$

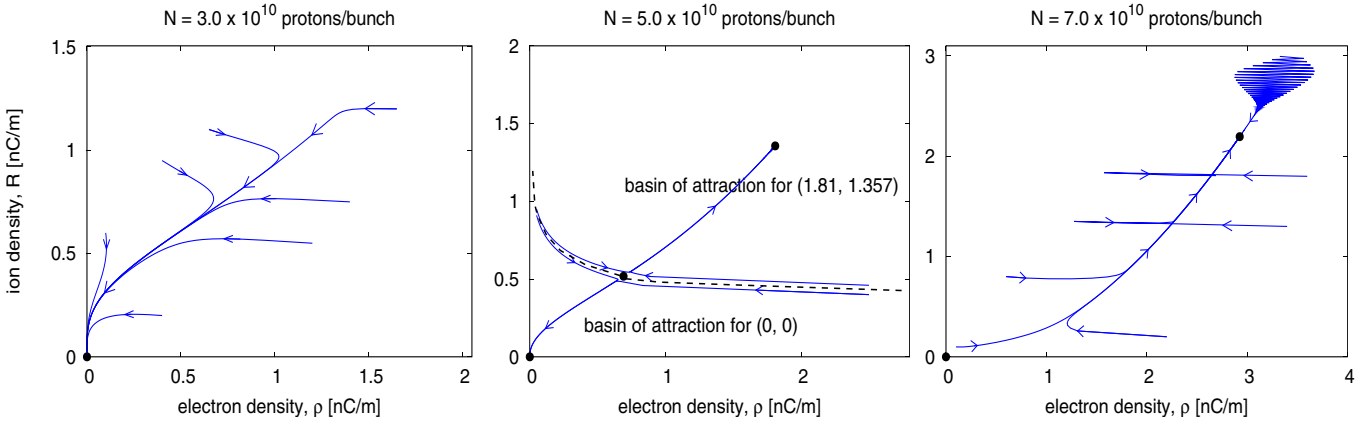

FIG. 7. (Color) Coupled motion in (ρ, R) space is tracked following the coupled maps for $N = 3 \times 10^{10}$ protons/bunch (left plot), $N = 5 \times 10^{10}$ protons/bunch (middle plot), and $N = 7 \times 10^{10}$ protons/bunch (right plot). Only one fixed point—$\vec{r}^* = (0, 0)$—exists for $N = 3 \times 10^{10}$, which acts as a global attractor. There are two *basins of attraction* for $N = 5 \times 10^{10}$: one containing the fixed point $\vec{r}^*_1 = (0, 0)$, and the second containing $\vec{r}^*_3 = (1.81, 1.357)$. The fixed point $\vec{r}^*_2 = (0.69, 0.52)$ sits on the boundary between the two basins, acting as a global repeller. Thus, the system evolve towards $\vec{r}^*_1$ or $\vec{r}^*_3$, depending on the initial conditions. The fixed point $\vec{r}^* = (2.9, 2.17)$ is a global attractor for $N = 7 \times 10^{10}$ protons/bunch, and all trajectories converge to this point as $m \to \infty$. In this case the fixed point $(0, 0)$ is a repeller.

$$\Delta R/\Delta t = (A - 1)R + Y\rho, \tag{29}$$

where the nominal time step $\Delta t = 1$ corresponds to the passage of a single bunch. The coupled differential equations that are obtained in the limit that $\Delta t \to 0$ exhibit stable cloud solutions that conform to the classical stationary solutions of Eq. (25). By contrast, Fig. 6, with $\Delta t = 1$, shows agreement with the classical stationary stable solution (upper dashed line) only up to about $N = 8.0 \times 10^{10}$, above which different dynamical phases become active.

Figure 8 shows the evolution of the electron and ion clouds for different bunch populations, always starting with the same (arbitrary) initial cloud densities. The clouds decay away or build to stable solutions with $N = 3 \times 10^{10}$ or 6×10^{10} protons per bunch, respectively, consistent with classical expectations (see Fig. 6). However, the clouds evolve into a stable period-2 oscillation when $N = 9 \times 10^{10}$ protons/bunch. Figure 9 takes a closer look at the chaotic dynamics that evolve when $N = 12 \times 10^{10}$ protons per bunch. In these cases, a crucial effect of the coupling is to change the sign of the effective space charge coefficient b'—positive ions neutralize the negative space charge of the electrons, permitting different physical stationary solutions.

Difference equations are inherently richer than the analogous differential equations, in the dynamical behavior that they display. In this case, coupled maps enhance the generation of period doubling and chaos, behavior that does not occur in the smoothed world of differential equations. Such additional dynamical phases have not (yet) been observed in electron clouds in accelerators, but it is

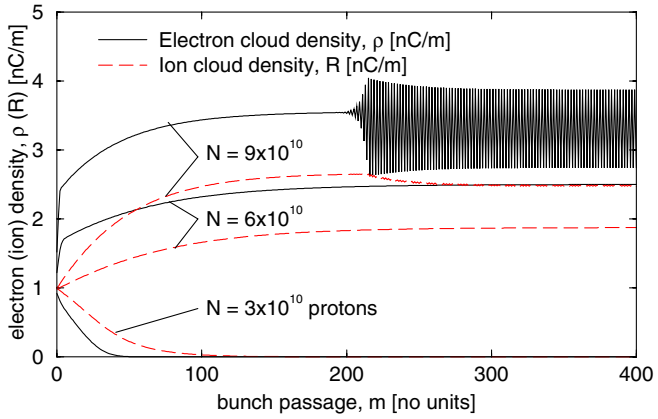

FIG. 8. (Color) Dynamical evolution of the electron and ion cloud densities as a function of time (bunch passage number) for 3 different bunch intensities, $N = 3 \times 10^{10}$, 6×10^{10}, and 9×10^{10} protons/bunch.

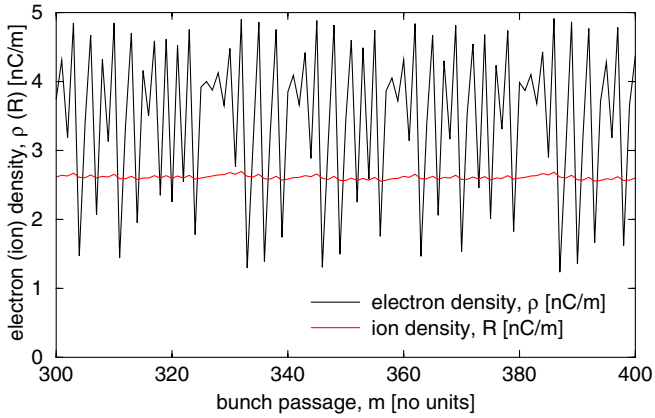

FIG. 9. (Color) Chaotic behavior of electron and ion cloud densities when $N = 12 \times 10^{10}$ protons per bunch.

possible they occur at, or near, typical operating conditions. An understanding of coupled cloud dynamics from the map perspective may prove important in enhancing accelerator performance.

V. CONCLUSIONS

Bunch-by-bunch maps are more appropriate than differential equations in modeling coupled cloud dynamics, because of the rapid evolution of the electron cloud—the high frequency components—after the violent transient of a bunch passage. In particular, the electron cloud energy spectrum changes enormously between bunch passages, with typical electron energies dropping from of order 1 keV to a only a few eV.

The ''proof-of-principle'' form of the coupled maps presented here can generate electron and ion clouds that turn on and off precipitously even with smooth and continuous dependence of the map coefficients (like the bunch to bunch gain a) on the electron cloud parameters (like the bunch intensity, N). Such first order phase transitions are sometimes seen in practice, but are beyond the capability of contemporary simulation codes, which model electron clouds in isolation. Other coupling mechanisms than those presented here are also plausible, and can be modeled within the same general map formalism.

ACKNOWLEDGMENTS

We wish to acknowledge the support of many people in the Collider-Accelerator Department at Brookhaven National Laboratory, including M. Blaskiewicz, W. Fischer, H. C. Hseuh, and S. Y. Zhang. We would like to especially thank the effort of P. Thieberger for his support and his enlightening discussions.

APPENDIX: LINEAR MOTION CONVERGENCE NEAR A FIXED POINT

The 2 by 2 Jacobian matrix J from Eq. (14) at the fixed point can be decomposed as

$$J = \sqrt{\det(J)}M_1, \tag{A1}$$

where M_1 is a unimodular 2 by 2 matrix, with

$$\det(M_1) = 1. \tag{A2}$$

Since J is a real matrix, then either $\sqrt{\det(J)}$ and M_1 are both real, or they are both imaginary, depending on the sign of $\det(J)$.

Considering instead the two-step motion

$$\vec{r}_{n+2} = J^2\vec{r}_n \tag{A3}$$

and using the identity

$$\det(J^2) = \overset{2}{\det}(J) \tag{A4}$$

then the decomposition

$$J^2 = \det(J)M \tag{A5}$$

now conveniently guarantees that both M and

$$d \equiv \det(J) \tag{A6}$$

are always real, although d may be negative. The equation of motion is now solved simply as

$$\vec{r}_{2n} = d^n M^n \vec{r}_0. \tag{A7}$$

The question now is ''how does M^n behave?''

Next, solve for the two eigenvalues of M, λ_- and λ_+, in the equation

$$M\boldsymbol{v} = \lambda\boldsymbol{v}, \tag{A8}$$

where $\boldsymbol{v}_-$ and $\boldsymbol{v}_+$ are the eigenvectors. In other words

$$\det(M - \lambda I) = 0, \tag{A9}$$

which is solved by

$$\lambda_\pm = \tfrac{1}{2}[\mathrm{Tr}(M) \pm \sqrt{\mathrm{Tr}^2(M) - 4}]. \tag{A10}$$

For convenience, introduce the notation

$$T(A) \equiv \tfrac{1}{2}\mathrm{Tr}(A), \tag{A11}$$

where A is a general matrix, so that the eigenvalues are written more compactly as

$$\lambda_\pm = T(M) \pm \sqrt{T^2(M) - 1}. \tag{A12}$$

There are now two possibilities— either the two-step motion represented by M is elliptical, or it is hyperbolic.

1. Elliptical motion

The easiest case is if

$$T^2(M) < 1. \tag{A13}$$

In this case the eigenvalues are both complex, with unit length

$$|\lambda_\pm| = 1 \tag{A14}$$

so that motion is elliptical around the fixed point, spiraling in to converge on the fixed point if

$$|d| < 1 \tag{A15}$$

or spiraling out and ''escaping'' if

$$|d| > 1. \tag{A16}$$

2. Hyperbolic motion

Slightly more complicated is the case if

$$T^2(M) > 1. \tag{A17}$$

In this case the eigenvalues are both real and the motion is hyperbolic around the fixed point. If the initial vector is decomposed as

$$x_0 = c_- v_- + c_+ v_+, \tag{A18}$$

then for arbitrary n

$$x_{2n} = d^n (c_- \lambda_-^n v_- + c_+ \lambda_+^n v_+). \tag{A19}$$

As time goes to infinity $n \to \infty$ the eigenmode with the larger absolute eigenvalue

$$|\lambda_1| = |T(M)| + \sqrt{T^2(M) - 1} \tag{A20}$$

comes to dominate, so that

$$x_{2n} \approx c_1 (d\lambda_1)^n v_1. \tag{A21}$$

This shows that, even though the motion is hyperbolic, it will still converge to the fixed point if (and only if)

$$|d\lambda_1| < 1. \tag{A22}$$

Using the substitution

$$T(M) = \frac{T(J^2)}{d}, \tag{A23}$$

this condition is rewritten to explicitly depend only on J, as

$$|T(J^2)| + \sqrt{T^2(J^2) - d^2} < 1. \tag{A24}$$

3. Summary

With the convenient definitions

$$t \equiv \frac{\mathrm{Tr}(J^2)}{2} \tag{A25}$$

$$d \equiv \det(J). \tag{A26}$$

Then, if

$$t^2 < d^2 \tag{A27}$$

the motion is elliptical, converging to the fixed point if

$$d^2 < 1. \tag{A28}$$

On the other hand, motion is hyperbolic if

$$t^2 > d^2. \tag{A29}$$

but nonetheless still converges to the fixed point if

$$|t| + \sqrt{t^2 - d^2} < 1. \tag{A30}$$

If neither of these pairs of conditions applies, then the motion diverges from the fixed point.

[1] W. Fischer, M. Blaskiewicz, M. Brennan, and T. Satogata, Phys. Rev. ST Accel. Beams **5**, 124401 (2002).

[2] V. Baglin and B. Jenninger, Phys. Rev. ST Accel. Beams **6**, 063201 (2003).

[3] F. Zimmermann, Phys. Rev. ST Accel. Beams **7**, 124801 (2004).

[4] U. Iriso, Ph.D. thesis, University of Barcelona, 2006.

[5] F. Zimmermann *et al.*, in Proceedings of EPAC'04, THPLT017, Lucerne, 2004. See also http://wwwslap.cern.ch/collective/ecloud02/ecsim.

[6] U. Iriso and S. Peggs, Phys. Rev. ST Accel. Beams **8**, 024403 (2005).

[7] U. Iriso and S. Peggs, C-AD/AP/147, Upton, 2004.

[8] U. Iriso and W. Fischer, Phys. Rev. ST Accel. Beams **8**, 113201 (2005).

[9] K. Harkay and R. A. Rosenberg, Phys. Rev. ST Accel. Beams **6**, 034402 (2003).

[10] R. Cimino, I. Collins, M. Furman, M. Pivi, F. Ruggiero, G. Rumolo, F. Zimmermann, Phys. Rev. Lett. **93**, 014801 (2004).

[11] M. A. Furman and M. Pivi, Phys. Rev. ST Accel. Beams **5**, 124404 (2002).

[12] G. Rumolo and F. Zimmermann, CERN-SL-2001-014 AP, 2001.

[13] W. Fischer, U. Iriso, and E. Mustafin, in Proceedings of the ICFA Workshop on High Intensity and High Brightness Hadron Beams, Bensheim, 2004.

[14] O. Gröbner, in Proceedings of the CARE HHH-2004 Workshop, Geneva, 2004.

[15] P. A. Redhead, J. P. Hobson, and E. V. Kornelsen, *The Physical Basis of Ultrahigh Vacuum*, High Vacuum Series, edited by L. Holand (Chapman and Hall, London, 1968), Chap. 4, p. 187.

[16] P. Thieberger, U. Iriso, and S. Peggs, C-A/AP/197.